Chapter 1

Basics of I-III-VI_2 chalcopyrites and solar cells

The semiconductor compound $CuGaSe_2$ belongs to the family of I-III-VI_2 chalcopyrites. This chapter begins with a brief overview of the material properties, highlighting those aspects that will be relevant later on for the discussion of the experimental results. In Section 1.2 the basic principles of photovoltaic devices based on p-n junctions are introduced, providing the reader with the fundamental concepts involved in the operation of conventional solar cells. Closing the chapter, Section 1.3 summarises the processing steps followed to fabricate the thin-film solar cells studied in this work.

1.1 Basics of I-III-VI_2 chalcopyrites

The chalcopyrite structure, named after the mineral chalcopyrite $CuFeS_2$ and also adopted by a number of I-III-VI_2 and II-IV-V_2 [10] compounds, is a ternary-compound equivalent of the diamond structure, in which every atom is bonded to four first-neighbours in a tetrahedral structure following the Grimm-Sommerfeld rule of chemical bonding[11], as schematically shown in Figure 1. The atomic bonds are mainly covalent, as expected from the strong tendency of Group IVa atoms tetrahedrally coordinated, like Si and Ge, to form sp^3 hybrid bonds. However, the presence of *d*-states from the Group Ib element contributing to the valence band via *p*-*d* hybridisation[12,13,14,15] introduces some ionic character in the chemical bonds[16,17] of I-III-VI_2 materials, like $CuGaSe_2$ (CGSe), which not only play an important role in the bulk properties of these compounds[10,18,19,20,21,22,23], but may also determine to some extent deviations from stoichiometry commonly encountered at their surfaces, as discussed below.

Ideally, each cation in the CGSe crystal is bonded to four anions and each anion in turn bonded to two pairs of different cations, forming a regular tetrahedron, as shown in Figure 1, like in the binary analogue zincblende. The alternate disposition of the two cation species Cu and Ga would therefore result in a unit cell twice as large in the *c*-direction as that corresponding to the zincblende, but the different characteristic strengths of Cu-Se and Ga-Se bonds[24] generate a tetragonal distortion of the unit cell by which $c<2a$ ($c/a \sim 1.966$). The bond angles in the tetrahedron are different from each other[25] (Cu-Se-Ga ~ 110.4°, Cu-Se-Cu ~ 107.0° and Ga-Se-Ga ~ 111.0°), resulting from a slight displacement *u* of the anion sites from their ideal positions[26], according to[19]:

$$u = \frac{1}{4} + \frac{R_{Ga-Se}^2 - R_{Cu-Se}^2}{a^2} \qquad \text{Eq. 1}$$

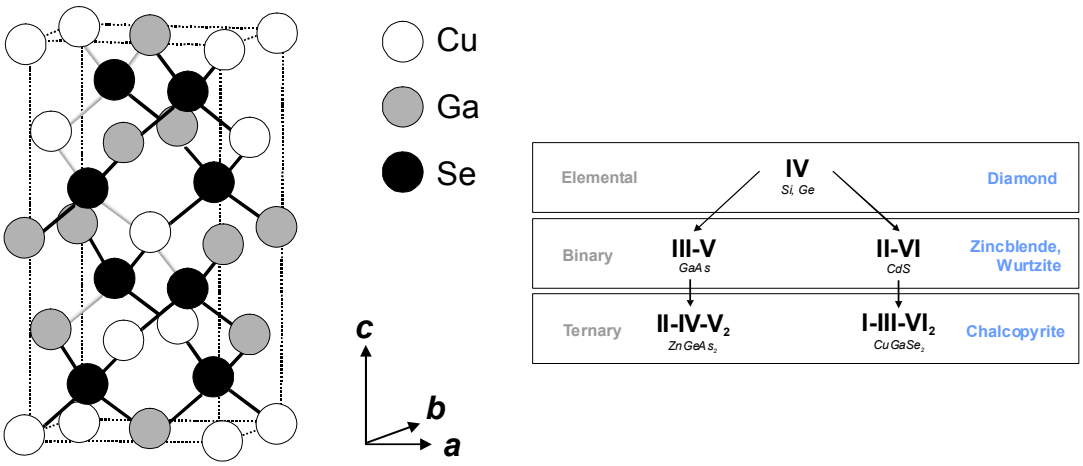

Figure 1. (Left) The tetragonal unit cell of $CuGaSe_2$, showing the chalcopyrite structure and the corresponding unit vectors, with |**a**| = |**b**| = 5.612 Å and |**c**| = 11.032 Å. **(Right)** Schematic illustration of the formation of ternary chalcopyrites from tetrahedrally coordinated Group IVa elements following the Grimm-Sommerfeld rule (four electrons per atom) from elemental to binary and ternary compounds. Common crystal structures and representative compounds are included.

where *R* denotes the characteristic bond length of the given species, *a* is the modulus of the unit vector, and *u* the anion displacement, estimated[25] for CGSe as 0.259±0.004 (*u*=0.25 corresponding to the ideal zincblende structure). The tetragonal distortion converts this material into uniaxially birefringent, contrarily to the binary analogues with cubic and hexagonal structures[27], where this effect is either absent or far too small for practical applications. Thus, in addition to photovoltaics, chalcopyrites have attracted attention from the field of non-linear optics[10,28,29].

The combination of the two mentioned effects, namely the tetragonal distortion of the unit cell and the incorporation of electronic *d*-levels from Cu to the valence band, provides characteristic features in the valence band density of states of this compound. On the one hand, the departure from cubic symmetry introduces a crystal-field interaction, which partly removes the triple degeneracy of the valence band. Further splitting results from spin-orbit interactions, accounting for three different direct band gaps, as schematically shown in Figure 2, according to[30]:

$$E_{1,3} = E_2 - \frac{1}{2}(\Delta_{so} + \Delta_{cf}) \pm \frac{1}{2}\sqrt{(\Delta_{so} + \Delta_{cf})^2 - \frac{8}{3}\Delta_{so}\Delta_{cf}} \qquad \text{Eq. 2}$$

where Δ_{so} and Δ_{cf} are, respectively the spin-orbit and crystal-field splittings (0.23 eV and –0.09 eV for CGSe, after [10]), and $E_{1,2,3}$ refer to the transitions A, B and C shown in Figure 2.

On the other hand, *p-d* hybridisation resulting from the incorporation of five-fold degenerate Cu-*d* orbitals into the valence states modifies the expected position of the top valence band. In the case of CGSe, Cu-*d* levels remain mostly in the deeper (bonding) range of the valence band, whereas the uppermost density of states at the valence band edge (anti-bonding) is of original *p*-character, provided by anions.

According to the standard molecular orbital interpretation[31], bonding and anti-bonding states repel each other in the energy axis in an amount inversely proportional to the energy difference between the original non-interacting *p* and *d* levels. Thus, the valence band edge mainly formed from anti-bonding states will be shifted upwards in the energy axis with respect to the situation where *d*-states were absent. This interpretation, derived from first-principle calculations[32] and supported experimentally by studies on various I-III-VI_2 compounds[33], partly accounts for the so-called band-gap anomaly of ternary compounds[19], namely, a considerable reduction of the energy band-gap in the transition from binary to ternary compounds sketched in Figure 1.

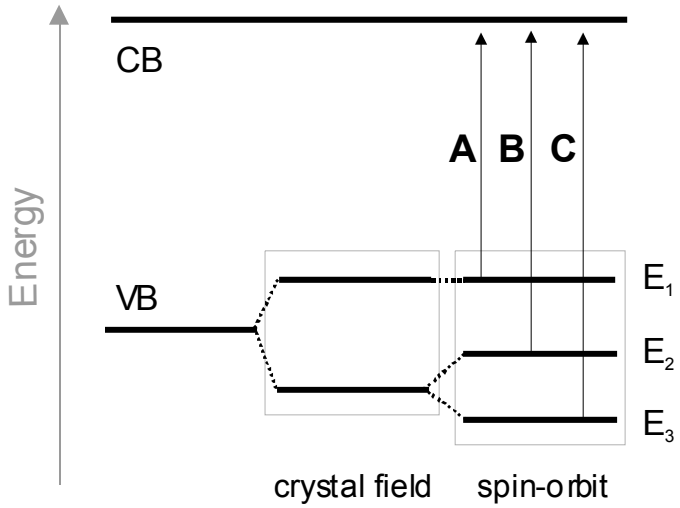

Figure 2. Schematic overview of the valence band of CGSe and the effects of the tetragonal crystal field and spin-orbit splitting. Direct transitions A, B and C determine the three direct band-gaps.

The electronic properties of CGSe, and other chalcopyrite compounds, are determined to a large extent by the presence of intrinsic defects in their crystalline structures. This is due to the extraordinary structural tolerance shown by these compounds regarding disorder in the lattice sites. As an example, single phase CGSe is found even in samples showing up to 10 mol% deviations from the ideal 1:1:2 stoichiometry towards the Ga_2Se_3 side of the pseudo-binary cut Cu_2Se-Ga_2Se_3 in the phase diagram[34]. This structural tolerance enhances, however, the sensitivity of the electronic parameters (in particular the doping concentration) with respect to the sample composition, as changes in the doping concentration of the order of $\pm 10^{19}$ cm^{-3} are associated with deviations from stoichiometry of just 0.1 at%.

The defect chemistry of ternary compounds is complex[35]. Considering just point defects in CGSe, up to 12 different intrinsic defects may appear:

- 3 vacancies: V_{Cu}, V_{Ga}, V_{Se}.
- 3 interstitials: Cu_i, Ga_i, Se_i.
- 6 antisites: Cu_{Ga}, Cu_{Se}, Ga_{Cu}, Ga_{Se}, Se_{Cu}, Se_{Ga}.

The occurrence of these defects in the actual CGSe structure will depend on the enthalpy of formation of each type of defect under given growing conditions, and on additional intrinsic self-compensating mechanisms, by which the formation of certain defect types favours in turn the appearance of a second type of defect of opposite electrical character (donor- or acceptor-like), leading to defect pairs of overall neutral character. Values of enthalpies of formation of intrinsic defects in CGSe were first reported by Neumann[36], based on theoretical calculations. From this study it was concluded that both vacancies and antisites are most likely to dominate the defect chemistry of the compound, as higher enthalpies of formation were systematically found for interstitials. In particular, copper vacancies V_{Cu} have been proposed by different authors as the dominant defect type of Cu-containing chalcopyrites, controlling its acceptor doping concentration, and therefore its p-type character, as well as the self-compensating mechanisms mentioned above, as inferred from first-principle calculations[37] and studies on samples grown from a variety of deposition processes. This last point, however, also plays an important role, specially in deposition processes based on chemical transport considered in this work, as the chemical species acting as transport agents modify the free energy and enthalpies of formation of different phases and intrinsic defects during the sample growth, compared to the situation in systems governed by vacuum conditions, like physical evaporation (PVD). In particular, Meeder[38] has recently presented a defect model for CGSe based on photoluminescence, optical and photoelectron spectroscopy studies, which explicitly takes into account the presence of iodine (used as transport agent in chemical vapour deposition (CVD) processes) in relation to the formation of Ga-vacancies in CVD-grown CGSe. Aspects of the defect chemistry are thus characteristic of the growth system employed for film deposition.

An interesting aspect of CGSe compared to other members of the chalcopyrite family, like $CuInS_2$ and $CuInSe_2$ is the failure to achieve intrinsic n-type conductivity in it. Only single-crystalline samples extrinsically doped by means of Ge-implantation and subsequently annealed under Zn-rich atmosphere were reported to show n-type conductivity[39]. This result is in agreement with theoretical calculations based on the *doping pinning rule*, first proposed by Walukiewicz[40], which predict the formation of neutral defect complexes, of the type $2V^{-}_{Cu}+Ga^{2+}_{Cu}$ in the case of study, as a function of the Fermi level position within the band-gap[41], inhibiting the continuous increase of n-character by simply increasing the corresponding density of donor-like defects in conditions close to equilibrium. Thus, only far from equilibrium (and ion implantation definitely provides a means for that) could in principle the n-type conductivity be achieved in CGSe, as long as those conditions prevent the activation of self-compensation mechanisms. This asymmetry in the p and n dopability is found in a variety of wide band-gap materials, being related to the absolute position the valence band maximum and conduction band minimum occupy with respect to a common energy reference (e.g. the vacuum level)[42]. Again, *p-d* hybridisation of valence states is partly responsible of this effect in I-III-VI_2, as it determines the position of the valence band maximum, as discussed above. Additionally, the lowering of defect formation enthalpies leading to neutral defect pairs as a function of the position of the Fermi level determines the morphology and faceting of certain crystal habits found on the samples as a function of their composition, as discussed by Jaffe et al.[43] in relation to the improved PV performance reported on devices based on films with preferential non-polar orientation[44]. Experimental evidences supporting the predictions of the doping pinning rule model have been reported from phototransport[45] and photoelectron spectroscopy studies[46] on different chalcopyrite compounds.

Ordered or disordered arrays of vacancies occupying the cation sites and related defect complexes can exceed the local range of the unit cell, leading to the field of the so-called *vacancy compounds*, first postulated by Pamplin[47]. Long-range ordering of vacant sites in periodic arrays of defects results in superlattice structures of the ideal chalcopyrite, reported as stable phases of ordered-vacancy compounds (OVC)[48]. The presence of such defected compounds segregated at surfaces of Cu-poor chalcopyrites has deserved some attention in the last years, as slightly Cu-poor compositions are routinely utilized in chalcopyrite films for photovoltaic applications. In fact, experimental evidence of their presence and of the active role these phases play in the solar cell performance[49] has been collected and nowadays the OVC is included in any energy band diagram depicting a $Cu(In,Ga)(Se,S)_2$-based solar cell.

In the case of CGSe, deviations from bulk composition have been repeatedly found at the surface of Cu-poor samples grown by different methods, including open-tube CVD-grown samples[50], pointing either to $CuGa_3Se_5$[51,52] or $CuGa_5Se_8$[53,54] phases segregated on the surface. 1:3:5 and 1:5:8 compositions are typical of chalcopyrite-related OVCs. Bulk crystalline samples of $CuGa_3Se_5$ have been grown and characterised[55], showing an enlarged band-gap of 1.75 eV compared to $CuGaSe_2$. Interestingly, $CuGa_3Se_5$ has been reported to show n-type conductivity[56], thus opening the possibility of shifting the metallurgical p-n junction of the solar cell, as explained in the next section, from the absorber/buffer interface to the inner bulk/surface absorber interface, likely reducing the interface recombination dominating most heterojunctions. Type inversion in CGSe could thus, in principle, be achieved in the surface region of Cu-poor samples. Whether this is the actual case or not, remains controversial in the literature, as no evidence so far for n-type conductivity at the surface of Cu-poor CGSe samples has been reported from photoemission studies. It is inferred that a defect compound with a composition close to 1:3:5 is effectively segregated at the surface, but likely showing a disordered structure.

This completes the overview on the material properties of CGSe and related compounds. We will return to some aspects of secondary phases segregating during the growth of CGSe films in Chapter 3, where their effects on the subsequent device processing and operation will be discussed.

1.2 Basics of solar cells

A solar cell can be conceived as a device in which photons from an illumination source are fed in and from which electrons are taken out to an external electric circuit. This simple picture, although still requiring a major polishing in order to gain some scientific respect, is indeed very accurate regarding the description of the fundamental aspects taking place in the materials from which standard devices are made. In other words, photon-electron interactions, as well as statistics and transport phenomena of free charge carriers in the absorber material, constitute the main physical processes involved in the performance of a solar cell.

The basic device requirements for photovoltaic energy conversion based on conventional solid-state designs are, first, to begin with a material whose free charge

carrier concentration can be easily modulated by illumination (semiconductors, by definition, fulfil this requirement, and high absorption coefficients are desirable); and second, to count with an asymmetry in the electrical properties of the semiconductor structure to be used as a solar cell. The latter can be accomplished by bringing together two semiconductors of opposite conductivity type, i.e. a semiconductor whose conductivity is controlled by the density of free holes in the valence band and a second semiconductor whose conductivity is controlled by the density of free electrons in the conduction band. The resulting transition region between them builds up a rectifying and photosensitive p-n junction, the key element for the transformation of the solar energy into electricity. In the following, the basic concepts on the formation and operation of p-n junctions will be reviewed and some important analytical expressions will be derived. The reader is referred to general references on the p-n junction theory (e.g. [57, 58, 59]) for further details.

Illuminating a piece of semiconductor material with photons of appropriate energy generates effectively an excess of charge carriers via the creation of electron-hole pairs, which are the components of the subsequent electronic transport. The photogeneration brings the semiconductor out from its equilibrium situation[60] regarding the electrochemical potential[a], assuming no other external bias (e.g. voltage bias) is applied to it. The first consequence of illuminating is thus that the distribution of free charge carriers is altered as result of the creation of electron-hole pairs. The excess free carriers, both of majority and minority type, will follow independent distributions according to the illumination conditions (in particular, the energy threshold of the impinging photons, transient or steady-state illumination conditions, etc.) and the availability of electronic states both in the valence and conduction bands. Nevertheless, the intuitive idea behind the concept of the Fermi level under equilibrium conditions (see the footnote), that of an electronic state characterised by an occupation probability of one half, is still useful even under non-equilibrium conditions like this, giving rise to the concept of *quasi*-Fermi levels. Each carrier type will then be characterised by its quasi-Fermi level, which is no longer constant, but a function of the position in the semiconductor, with both the electron and hole quasi-Fermi levels ending up as a single Fermi level in equilibrium after the transient effects of switching off the illumination fade away. The splitting of quasi-Fermi levels under non-equilibrium conditions is a direct measurement of the maximum obtainable output voltage from the device.

It is the minority carrier concentration that suffers major changes under illumination, assuming low injection levels (i.e. if the number of photogenerated electron-hole pairs is of the order of the free carrier concentration in darkness provided by the doping). These photogenerated minority carriers will undergo recombination processes if no means of charge separation is implemented in order to avoid it. A way to do so consists in transforming *minority* carriers into *majority* carriers, a process which must be accomplished within the minority carrier lifetime after the photogeneration event. This is the basic function of a p-n junction, the provision of a means to separating charge carriers by injecting minority carriers generated on one side of the junction into the side of opposite character, where they act in turn as majority carriers. This is achieved by an internal electric field present at the transition region, which sweeps the charge carriers

[a] Strictly speaking, a p-n junction is *not* in thermodynamical equilibrium, as different concentrations of species (i.e. free electrons and holes) are present on either side of the junction. However, equilibria may exist with respect to a *certain* variable in the general expression of the free energy $dF(T, V, N_i, Q, \ldots)= -SdT-pdV+\Sigma\mu_i dN_i+\varphi Q+\ldots$; in particular, to the electrochemical potential $\eta=\mu+q\varphi$, referred to as the Fermi energy: $E_F = \eta$. For a detailed discussion, see Ref. [60].

in opposite directions, according to their charge type. A p-n junction is thus a minority carrier device, in the sense that it is the minority carrier concentration on each side of the junction that controls the electronic transport responsible for its performance.

The electric field at the junction builds up as a result of the different electrochemical potentials of electrons and holes on either side of the p-n junction. A non-degenerate p-type semiconductor is characterised by the position of its Fermi level E_F within the band gap as a function of the net ionised acceptor doping concentration N_A^-, according to:

$$p = N_V e^{-(E_F - E_V)} \qquad \text{Eq. 3}$$

where p is the free hole concentration, $p = N_A^-$, N_V is the so-called effective density of states at the valence band edge, and E_V is the edge of the valence band. On the *n*-type side, it holds that:

$$n = N_C e^{-(E_C - E_F)} \qquad \text{Eq. 4}$$

where n is the free electron concentration equal to the net ionised donor doping concentration, $n = N_D^+$, N_C is the effective density of states at the conduction band edge, and E_C is the edge of the conduction band. In the case of a degenerate semiconductor, Boltzmann statistics implicitly assumed in Eqs. 3 and 4 must be replaced by Fermi-Dirac statistics, which in first approximation leads to the following expression for a degenerate *n*-type material[61]:

$$E_F - E_C \approx \left(\frac{\hbar^2}{2m_e^*} \right) \left(3\pi^2 n \right)^{2/3} \qquad \text{Eq. 5}$$

where m_e^* denotes the electron effective mass in the conduction band. The different concentrations of electrons and holes on either side of the junction induce diffusion currents of electrons to the *p*-side and holes to the *n*-side when both materials are brought in contact, tending to equalise the charge carrier concentrations throughout the entire device. However, due to the fact that the diffusion process of free carriers is accompanied by a net charge transfer, the thermodynamic equilibrium is not reached with respect to the chemical potential (number of particles), but to the electrochemical potential (number plus charge of particles), i.e. the Fermi level. The reason behind this is that every carrier diffusing from one side of the junction to the other leaves behind unbalanced charge localised at the ionised impurity from which the free carrier was originally released.

Charge of opposite sign builds up thus in the nearby region of the metallurgical junction, and the process goes on until the Fermi level aligns itself all through the device, provided that no external bias (light, voltage, temperature gradient, etc.) is applied to the sample, as can be seen in Figure 3. The fixed charge density $\rho(x)$

associated to the unbalanced ionised impurities N_A^- and N_D^+ induces an electric field, which can in principle be calculated by means of Gauss' law[b]:

$$E(x) = \frac{1}{\varepsilon\varepsilon_0}\int_{-\infty}^{x}\rho(x)dx \qquad \text{Eq. 6}$$

where ε is the relative dielectric constant of the material and ε_0 is the permittivity of free space. This electric field counteracts the diffusion process originating from the different concentration gradients of electrons and holes on either side of the junction. A steady-state situation is achieved, where diffusion and electrical drift of free charge carriers across the junction in opposite directions compensate each other. From electromagnetic field theory, the electric field $\boldsymbol{E}$ is related to the gradient of the electrostatic potential V by:

$$\mathbf{E}(x) = -\nabla V(x) \qquad \text{Eq. 7}$$

which substituted in Eq. 6 leads to Poisson's equation:

$$\frac{\partial^2 V(x)}{\partial x^2} = -\frac{\rho(x)}{\varepsilon\varepsilon_0} \qquad \text{Eq. 8}$$

In practice, it is the electrostatic potential $V(x)$ which is used as starting parameter for the subsequent analysis, as it is easily incorporated in the band diagram of the heterostructure, as shown in Figure 3.

Unfortunately, Poisson's equation is not easy to solve in its exact from. In order to end up with closed-form solutions for V and $\boldsymbol{E}$ as functions of x, some approximations must be introduced in Eq. 8, regarding the dependence of the charge distribution on the position. A particularly useful approach is known as the *depletion approximation*, introduced by Schottky[62], which assumes that the presence of free mobile carriers within the transition region at the junction is negligible (the *depletion region*) compared to the donor and acceptor ion concentrations on either side, the device being neutral elsewhere. Implicitly it also assumes the validity of Boltzmann's statistics, kT/q being much smaller than any potential drop across the junction, which is essential to the concept of a well-defined depletion width.

[b] One-dimensional models are assumed hereafter in the entire work for the sake of simplicity in the derivation of analytical expressions, where the variable x must be understood as the spatial direction perpendicular to the metallurgical junction plane at any particular position. This is clearly only a crude approximation since real devices are three-dimensional (the metallurgical junction being not constrained to an ideal algebraically defined flat plane, but occupying a certain volume), and it will be justified only if the major variables included in the analysis change rapidly just in one spatial direction (which may not always be the case, in particular in polycrystalline materials with significant surface roughness). Nonetheless, effects related to the higher dimensionality of the interface will be considered as a correction to the first order approximation of the one-dimensional model, as long as the latter accounts satisfactorily for the phenomena under study.

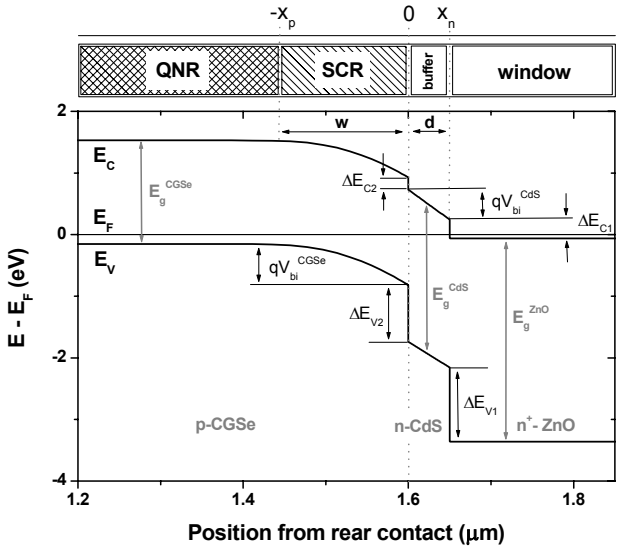

Figure 3. Schematic cross-section of the semiconductor heterostructure **(upper)** and related band diagram of a CGSe-based thin-film solar cell **(lower)**. The p-n junction is located at the interface between the p-type CGSe absorber on the left side and the thin n-type CdS buffer layer

This approximation states that the semiconductor on either side of the p-n junction can be divided into two different regions, as depicted in Figure 3, the transition region, hereafter referred to as the *space-charge region* (SCR), which is totally depleted of free carriers, and the bulk *quasi-neutral region* (QNR), which is everywhere electrically neutral. The interface between these two regions is abrupt, defining the SCR edges, down to the Debye screening length L_D:

$$L_D = \sqrt{\frac{kT\varepsilon\varepsilon_0}{q^2 N}} \qquad \text{Eq. 9}$$

where N denotes in this expression the net doping concentration, either donors or acceptors on each side of the junction. Actually, the spread out of free carriers around the SCR edge normally takes place over distances of a few Debye lengths[63]. The depletion approximation leads to a general expression of Poisson's equation:

$$V_{bi}(x) = \frac{1}{\varepsilon\varepsilon_0}\int_{-x_p}^{x_n} x\rho(x)dx \qquad \text{Eq. 10}$$

where $V_{bi}(x)$ represents the built-in potential at the junction (i.e. q times $V_{bi}(x) = V_{bi}^{CGSe} + V_{bi}^{CdS}$ is the total band bending across the junction in the band diagram of Figure 3), and $-x_p$, x_n denote the SCR edges. This equation relates the SCR width to the total electrostatic potential across the junction and the space charge distribution of unbalanced ions, and is valid provided that the device is electrically neutral, so that:

$$\int_{-x_p}^{x_n} \rho(x)dx = 0 \qquad \text{Eq. 11}$$

or in other words, the stored charge on the *n*-side of the SCR must be balanced by the same amount of charge of opposite sign on the *p*-side of the SCR. Analytical solutions of Eq. 10 can be found for the case of uniform doping concentration, leading to:

$$w = x_n + x_p = \sqrt{\frac{2\varepsilon\varepsilon_0 V_{bi}}{q}\left(\frac{1}{N_A^-} + \frac{1}{N_D^+}\right)} \qquad \text{Eq. 12}$$

which gives the SCR width w as a function of the doping concentrations and the total potential drop across the junction. The band bending as a function of the position is given by:

$$V(x) = E_m\left(x - \frac{x^2}{2w}\right) \qquad \text{Eq. 13}$$

where E_m is the maximum electric field, achieved at the metallurgical junction, given by:

$$|E_m| = \frac{qN_D^+ x_n}{\varepsilon\varepsilon_0} = \frac{qN_A^- x_p}{\varepsilon\varepsilon_0} \qquad \text{Eq. 14}$$

In the frame of the depletion approximation, any external voltage applied to the p-n junction will drop only within the SCR, as this is the highest resistive region due to the absence of free charge carriers. This simple picture neglects the voltage drop in the QNR, compared to that in the SCR. In fact, there will always be a certain voltage drop in the QNR when applying an external voltage to a piece of semiconductor (e.g. when measuring its resistivity), but it will be negligible compared to the potential drop in the SCR. With this assumption, the effect of an external bias V_{app} can be introduced in the analytical expressions derived so far by adding it to the built-in potential, according to:

$$V = V_{bi} \mp V_{app} \qquad \text{Eq. 15}$$

where the sign criterion states that an external forward bias reduces the built-in potential, whereas a reverse bias increases it. This can be understood, as reverse-biasing the junction increases the difference in electrochemical potentials between the n-type and p-type sides of the junction, and therefore larger fluxes of free carriers are driven to the opposite side, uncovering in turn a larger amount of fixed charge and increasing the SCR width. The opposite effect holds for the forward bias case.

A further simplification can be introduced in Eq. 12 if the doping concentration on one side of the junction clearly exceeds the concentration on the opposite side. If $N_D >> N_A$ as in a n^+-p heterojunction, or in the ideal case of a Schottky contact,

$$w \approx x_p = \sqrt{\frac{2\varepsilon\varepsilon_0 V_{bi}}{qN_A^-}} \qquad \text{Eq. 16}$$

holds, which states that the entire SCR width is dominated by the lightly doped side of the junction.

This completes the review on the basics of p-n junction formation. We turn now our attention to the properties of the p-n junction regarding the electronic transport, and particularly how the junction provides a means of separating generated electron-hole pairs by injecting minority carriers into the side of equal conductivity type.

Electron-hole pairs are constantly generated on either side of the p-n junction in equilibrium at a constant rate, due to the thermal energy provided by phonons. This means that at each instant there will be a certain number of majority carriers on the p-side with sufficient energy to overcome the built-in potential barrier and diffuse into the n-side, where they act as minority carriers. These carriers undergo recombination processes, as stated above, after a certain characteristic time, the minority carrier lifetime. Thus, a current density J_{pr} (defined as the total current I_{pr} per unit area of p-n junction) of holes diffusing from the *p*-side into the *n*-side, where they recombine, is established under equilibrium conditions (i.e V_{app}=0), this current being referred to as a *recombination* current. The principle of detailed balance[64], however, ensures that every microscopic transport phenomena must be compensated by its inverse process, both operating at the same rate, in order to maintain the equilibrium situation. In other words, no net current can be measured in a device in equilibrium. The inverse process of J_{pr} is the generation and subsequent diffusion of holes from the *n*-side into the *p*-side, favoured by the built-in potential, where they act as majority carriers. A current density J_{pg} of holes from the *n*-side into the *p*-side is established, referred to as a *generation* current. In equilibrium:

$$J_{pg} = -J_{pr} \qquad \text{Eq. 17}$$

holds. The same considerations apply to the case of electrons, with analogue generation and recombination current densities J_{ng}, J_{nr} leading to:

$$J_{ng} = -J_{nr} \qquad \text{Eq. 18}$$

and in equilibrium the net currents of electrons and holes across the junction are zero. Now, the characteristic feature of a p-n junction regarding the electronic transport under applied bias lies in the unbalance of generation and recombination currents under working conditions:

- Under reverse bias, the potential barrier at the junction increases according to Eq. 15. Under these conditions, diffusion of holes over the barrier from the *p*-side into the *n*-side, and of electrons from the *n*-side to the *p*-side, is inhibited, leading to small values of the recombination currents J_{pr} and J_{nr}. Generation currents J_{pg}, J_{ng} are, however, independent of the applied bias, depending exclusively on the thermal generation rate of electron-hole pairs in the vicinity

of the SCR, being a function of the energy band-gap of the material and the temperature to which the junction is subjected. As the reverse bias increases the unbalance between generation and recombination currents increases, building a small net current across the junction with a nearly constant value $-q(J_{pg}-J_{ng})$, referred to as the saturation current of the junction.

- Under forward bias the potential barrier is reduced (Eq. 15) and thus, recombination currents are favoured compared to the corresponding generation currents, which remain unaffected by the applied bias. The current consists of majority carriers diffusing over the barrier, becoming minority carriers on the opposite side of the junction. Recombination currents can be extremely large, being controlled by the carrier concentration with sufficient energy to surmount the decreasing potential barrier as a function of increasing forward bias. Assuming Maxwell-Boltzmann statistics, these carrier concentrations are proportional to:

$$n, p \propto e^{qV_{app}/kT} \qquad \text{Eq. 19}$$

and the same must hold for J_{nr} and J_{pr}, as they are functions of the potential barrier $q(V_{bi}-V_{app})$:

$$J_{nr}, J_{pr} \propto e^{qV_{app}/kT} \qquad \text{Eq. 20}$$

Now, with the condition $J_{pr} = J_{pg}$ and $J_{nr} = J_{ng}$ whenever the applied potential vanishes $V_{app}= 0$, the unbalance between generation and recombination currents of electrons and holes as a function of the potential barrier must follow:

$$J_{pr} = J_{pg} e^{qV_{app}/kT} \qquad \text{Eq. 21}$$

$$J_{nr} = J_{ng} e^{qV_{app}/kT} \qquad \text{Eq. 22}$$

and net electron and hole currents flow through the junction according to:

$$J_p = J_{pr} - J_{pg} = J_{pg}\left(e^{qV_{app}/kT} - 1\right) \qquad \text{Eq. 23}$$

$$J_n = J_{ng} - J_{nr} = -J_{ng}\left(e^{qV_{app}/kT} - 1\right) \qquad \text{Eq. 24}$$

The total current flowing across the junction will be thus given by:

$$J = q(J_p - J_n) = q\left(J_{pg} + J_{ng}\right)\left(e^{qV_{app}/kT} - 1\right) = J_0\left(e^{qV_{app}/kT} - 1\right) \qquad \text{Eq. 25}$$

where the J_0 denotes the saturation current density $q(J_{pg}+J_{ng})$. An alternative approach for the derivation of Eq. 25, solving the continuity equation for charge carriers (see Section 2.2.1) with the boundary conditions derived from the

depletion approximation, leads to an analytical expression of the saturation current density that will be useful later on in Chapters 2 and 4:

$$J_0 = qn_i^2\left(\frac{D_n}{N_A L_n} + \frac{D_p}{N_D L_p}\right) = J_{00}\exp\left(-\frac{E_g}{kT}\right) \quad \text{Eq. 26}$$

where $D_{n,p}$ and $L_{n,p}$ denote the diffusivity and the diffusion length of minority electrons and holes on either side of the junction, and n_i denotes the intrinsic carrier concentration for a certain temperature T, given by:

$$n_i^2 = N_C N_V \exp\left(\frac{-E_g}{kT}\right) \quad \text{Eq. 27}$$

Eq. 25 is referred to as the diode equation, relating the current flowing through a p-n junction from which standard diodes are made of, as a function of the applied bias. The different impedance recorded in the junction under forward and reverse bias conditions is the principal feature of this type of device.

The basic principle of the p-n junction remains valid under illumination, when photogenerated pairs resulting from electron-photon interactions add themselves up to those generated thermally by electron-phonon interactions. Illuminating the device brings the junction out of equilibrium, as discussed above. Now, excess minority carriers compared to the case of the junction in equilibrium can diffuse favoured by the potential drop to the side of equal conductivity type. In other words, photogenerated carriers increase the generation currents. Even without any applied voltage V_{app}=0, there exists an unbalance of generation and recombination currents, building a net photogenerated current density J_{ph} across the junction. This means that if the illuminated junction is implemented in an electric circuit in short-circuit conditions, a net current will be measured as long as the junction is illuminated. In the same way, under open-circuit conditions, a potential difference between the two sides of the p-n junction is measured as a voltage. Clearly, an additional term must be included in Eq. 25 to account for the effect of the photogenerated current, leading to:

$$J = J_0\left(e^{qV_{app}/kT} - 1\right) - J_{ph}(V_{app}) \quad \text{Eq. 28}$$

where it is explicitly stated that the photogenerated current collected at the p-n junction contacts can be a function of the applied bias under given working conditions, as discussed in Section 2.2.2.

The performance of a solar cell can thus be monitored from its current-voltage characteristic (referred to as I-V or J-V curves, depending on whether speaking of total current [A] or current density [Acm^{-2}] as a function of the applied voltage). Essentially, it is the I-V curve of a diode for measurements in darkness, as shown in Figure 4. Repeating the measurement under illumination, a shift to negative current values is recorded in the characteristic, as a result of the additional photocurrent, corresponding

to the situation in which electrical power can be obtained from the device[c]. We will return to Eq. 28 in Chapter 2 when referring to the electronic characterisation of devices by means of I(V, T) analysis.

The output of a solar cell is measured as the ratio of the electrical power delivered by the device to an external circuit to the incoming power from the illumination source, according to:

$$\eta = \frac{P_{out}}{P_{in}} \qquad \text{Eq. 29}$$

where η is referred to as the energy conversion efficiency of the solar cell. The power output can be directly obtained from the I-V characteristic, according to:

$$P_{out} = V \cdot I \qquad \text{Eq. 30}$$

and it will be thus given at any operating point by the area of the rectangle enclosed by the corresponding point in the I-V curve and the axes, as shown in Figure 4. The power output will be maximum at one particular point given by I_{mpp} and V_{mpp} (where the subindex denotes *maximum power point*). Three parameters are commonly used to characterise the performance of the solar cell under given illumination conditions (see, for instance Ref. [65]):

- The short-circuit current I_{sc} (current at zero bias) ideally represents the photocurrent contribution to the electronic transport. This is the current circulating through an external circuit connected to the metal contacts of the solar cell under short-circuit conditions.
- The open-circuit voltage V_{oc} (voltage at which $I = 0$), is the maximum voltage obtainable from the device and, ideally, a measurement of the change in electrochemical potential of electrons and holes with respect to the equilibrium conditions in darkness.
- The fill factor *FF* of the I-V curve, defined as:

$$FF = \frac{V_{mpp} I_{mpp}}{V_{oc} I_{sc}} \qquad \text{Eq. 31}$$

  which can be understood as a measurement of the *squareness* of the I-V characteristic. Equivalently, it is the area ratio between the rectangle of maximal area enclosed by the axes and the experimental I-V (i.e. the maximum power point), and that enclosed by the axes and the corresponding parallels at I_{sc} and V_{oc} (see Figure 4). From Eqs. 29 and 31, the energy conversion efficiency of the solar cell can be written as:

$$\eta = \frac{V_{oc} I_{sc} FF}{P_{in}} \qquad \text{Eq. 32}$$

[c] For this reason, the fourth quadrant in the I-V plot is referred to as the *power quadrant.*

I-V analysis constitutes a powerful characterisation technique, not only to assess the quality of the solar cells, but also to study the limiting factors of their performance. This aspect will be revisited in Chapter 2.

This completes the review of the electronic operation of a p-n junction and related solar cells.

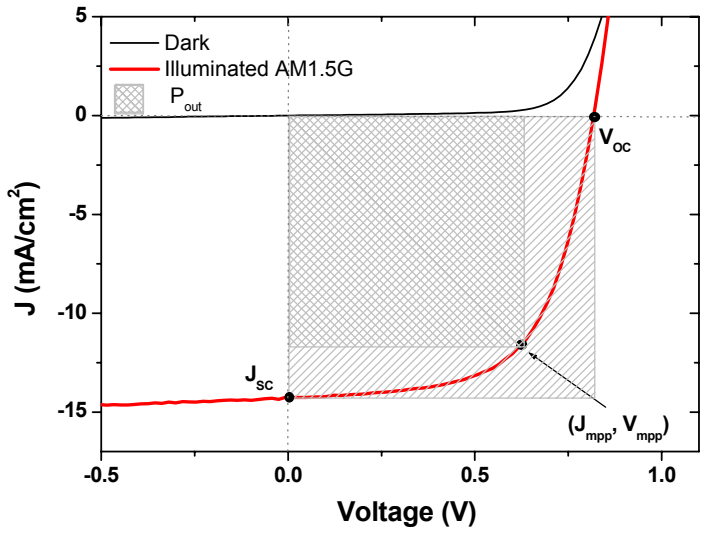

Figure 4. J-V characteristic of a CGSe-based thin-film solar solar cell in darkness and under illumination. The maximum power point (J_{mpp},V_{mpp}) corresponds to that point of the illuminated J-V in the power quadrant where the product J·V is maximum. The fill factor is defined as the area ratio of the two enclosed areas.

1.3 Preparation of solar cells based on $CuGaSe_2$

Chalcopyrite-based solar cells have demonstrated the highest energy conversion efficiency of thin-film technology, with figures close to 20 % in laboratory scale[7] from $Cu(In,Ga)Se_2$ absorbers. They consist of a stacked layer sequence of various compounds, with a total thickness not larger than a few microns (excluding the substrate).

Figure 5 shows a scheme of the typical structure of a chalcopyrite-based thin-film solar cell. Complete devices of this type studied in this work on the basis of CVD-grown CGSe absorbers are built in a series of steps, which are summarised in the following points:

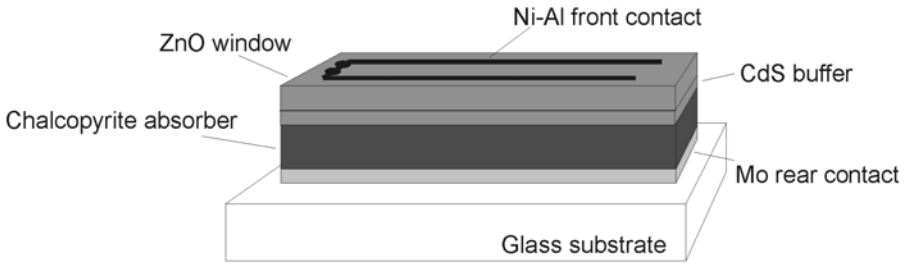

Figure 5. Schematic diagram of the layer sequence in a chalcopyrite-based thin-film solar cell. The thickness of different layers are not in scale (see text).

- A clean substrate, normally a piece of soda-lime glass (SLG), is coated either by evaporation or dc-sputtering with a 1 μm thick Mo film to provide the device rear contact. The sheet resistance of the Mo-coating lies between 50-250 μΩcm. The Na-content of the glass (typically ~12% in the form of Na_2O in commercial SLG) plays an important role during the absorber deposition, when the high processing temperatures activate Na-diffusion through the rear contact, being incorporated into the absorber. It has been experimentally observed that Na has beneficial effects on both the structural and electronic properties of $Cu(In,Ga)(Se,S)_2$ compounds, increasing the efficiency figures of final devices. Na-precursors on the Mo rear contact are also used in high efficiency devices as Na-source, for a fine control of its incorporation in the absorber film. Further details on the role of Na can be found in Refs. [66,67] and references therein. Regarding the rear contact, an ohmic behaviour with low contact resistance associated is desired in order to deliver the photocurrent from the device without significant losses. It will be discussed in Chapters 3 and 4 how the mediation of a $MoSe_2$ interfacial layer formed during the absorber deposition process can influence the electronics of the contact.

- The coated substrate is introduced in the deposition system, where the p-type absorber film is grown on top. The typical absorber thickness lies between 1 and 3 μm, in order to ensure on the one hand the complete absorption of that part of the sun spectrum with $h\upsilon > E_g$, and on the other hand to minimise the recombination of minority carriers at the rear contact. Typical conductivity values of CVD-grown CGSe films processed as solar cells lie in the range 10^{-2}-10^{-1} $\Omega^{-1}cm^{-1}$. Details of the deposition process used in this work and its optimisation will be given in Chapter 3.

- A chemical bath deposition (CBD) process follows, by which the so-called buffer layer is provided. This typically consists of a 50 nm thick CdS [d] lightly n-type semiconductor ($n \sim 10^{17} cm^{-3}$) with E_g=2.42 eV. Although all high-efficiency devices include a buffer mediating the p-n heterojunction, its role in

[d] The substitution of CdS as buffer by alternative materials, e.g. ZnSe, ZnS and $In_x(OH,S)_y$, is an active area in the field of thin-film photovoltaics, with a two-fold aim: eliminate Cd in the processing of environmentally friendly products and to develop dry processes for up-scaling production lines.

the device performance is still controversial. Detailed aspects related to the properties of the CBD-grown CdS buffer can be found in Ref. [68].
The CBD process is realised by means of a precipitation reaction taking place in an aqueous solution, with a cation source, in this work $Cd(AcO)_2$ (cadmium acetate), and an anion source, $(NH_2)_2CS$ (thiourea). The reaction takes place by the complexation of Cd by ammonia and the release of S by decomposition of the thiourea, as the solution is warmed up from 25°C to 60°C. CdS is formed in small crystallites precipitating on the absorber film, which is dipped in the solution during the warming up, providing a homogeneous and closed thin overlayer. The reader is referred to Ref. [66] for further details on the CBD process for the deposition of CdS on CGSe films.

- The n^+ heterojunction partner is provided by ac-sputtering of a double layer of the transparent conductive oxide (TCO) ZnO acting as a window, i.e. permitting the visible light to pass through with minor absorption losses and to reach the underlying absorber film. The window layer typically consists of an intrinsically doped i-ZnO layer of ~100 nm thickness and net doping concentration of $N_D \sim 5 \cdot 10^{17}$ cm^{-3}, and a highly doped Ga:ZnO of ~400 nm and $N_D \sim 1 \cdot 10^{20}$ cm^{-3} (see e.g. Ref. [69]). The intrinsic layer prevents Ga-diffusion into the buffer and reduces those losses associated to shunts in the p-n structure[70], whereas the high doping concentration of the Ga:ZnO ensures that the band bending associated to the p-n junction, according to Eq.16 and schematically shown in Figure 3, takes place to a large extent within the absorber for an optimal collection of photogenerated carriers.

- The front contact of the device is provided in the form of a metallic grid in order to minimise shadowing effects during device operation. A double layer of 10 nm Ni and 1 μm Al is evaporated on the window front surface. The thin Ni layer prevents the rapid oxidation of Al that would result from a direct contact with the ZnO window, whereas the Al layer provides the actual ohmic contact of the device.

Typical substrate areas used in this work are 2.5x2.5 cm^2. Once the device processing is completed, up to eight solar cells of 0.5 cm^2 are isolated by mechanical scribing, providing a number of samples from the same process for characterisation.